



Sensitivity analysis of geological parameters to evaluate uncertainty in underground hydrogen storage performance for a saline aquifer at Ketzin (Germany)

Lea Döpp · Anna-Maria Eckel ·
Márton Pál Farkas · Wolfgang Weinzierl ·
Cornelia Schmidt-Hattenberger · Ingo Sass

Received: 12 February 2025 / Accepted: 11 May 2025
© The Author(s) 2025

Abstract A numerical sensitivity analysis of a hydrogen pore storage system is carried out on a reservoir-scale geological model of the Ketzin site (Germany) to analyze the influence of uncertainty in geological parameters and fluid properties on storage performance. Therefore, the following physical geological parameters and fluid properties were investigated: Porosity and permeability of the reservoir rock, the brine salinity, relative permeability and capillary pressure and mechanical dispersion. The range of the applied parameters is based on experimental and field data of the chosen location obtained during the former CO₂ storage projects at the Ketzin site from 2008 to 2013. Using the open-source reservoir software MUFITS for the numerical simulations, strong differences between the results can be observed. The results were evaluated based on measures to quantify performance, such as the ratio of produced hydrogen mass to produced cushion gas (nitrogen), productivity index and sustainability index. The strongest impact on the performance parameters was observed with

variations in the capillary pressure and the relative permeability curves followed by the absolute permeabilities, while the least impact was seen with changes in the porosity and salinity of the brine. This work is not only crucial as a pre-feasibility study for the Ketzin storage site for hydrogen storage but also as a basis for decision-making for other potential storage sites in sedimentary basins.

Highlights

- A sensitivity analysis of hydrogen storage at Ketzin on geological parameters is considered.
- The open-source software MUFITS is utilized for reservoir-scale numerical simulations.
- Permeability and capillary pressure significantly affect storage performance.
- Recommendations for realizing a future hydrogen storage demonstrator are provided.

L. Döpp (✉) · A.-M. Eckel · M. P. Farkas · W. Weinzierl ·
C. Schmidt-Hattenberger · I. Sass
GFZ Helmholtz Centre for Geosciences, Section 4.3
Geoenergy, Telegrafenberg, 14473 Potsdam, Germany
e-mail: lea.doep@gfz.de

L. Döpp · I. Sass
Institute of Applied Geosciences, Geothermal Science
and Technology, Technical University Darmstadt,
Schnittspahnstraße 9, 64287 Darmstadt, Germany

Keywords Underground hydrogen storage ·
Numerical reservoir simulation · Sensitivity analysis ·
Saline aquifer · Geological porous media · Energy
storage

Abbreviations

α Dispersivity (m)

b	Salinity (mol/kg)
μ	Viscosity (Pa s)
ϕ	Porosity
ω_{H_2}	Gas mass fraction
BHP	Wellbore bottom-hole pressure (bar)
k_h, k_v	Horizontal, vertical permeability (mD)
k_r	Relative permeability
M	Mass (t)
p	Pressure (bar)
p_c	Capillary pressure (bar)
PI	Productivity index ($Sm^3/day/bar^2$)
Q	Mass ratio
SI	Sustainability index
S_g, S_w	Gas, water saturation
t	Time (day)
T	Temperature ($^{\circ}C$)

1 Introduction

To achieve climate neutrality, Germany has committed to energy transition as part of the Federal Climate Protection Act (German Federal Government 2019). As a key component of that, the national hydrogen strategy of the German Federal Ministry of Economic Affairs and Climate Action (2020) outlines targets for hydrogen (H_2) production, infrastructure, application and regulations. Central to this strategy is H_2 underground storage, which ensures supply security and enables dispatchable renewable energy. Surplus electricity is converted to green H_2 via electrolysis, allowing energy storage and later consumption.

H_2 storage can be realized with surface tanks providing capacities ranging from hours to days (kWh-MWh) (Sterner and Specht 2021). However, to achieve the abovementioned goals, capacities in the range of GWh to TWh over weeks to months are required, and therefore, subsurface storage is needed (Sterner and Specht 2021). Cavern storage facilities are primarily located in the northern regions of Germany (Kruck et al. 2013). On the other hand, depleted natural gas fields and saline aquifers are more abundant in Germany and throughout Europe (Heinemann et al. 2021a). In these cases, gas is stored in the pores of a geological reservoir, which are usually sedimentary rocks such as sandstone or limestone and provide a higher storage capacity than caverns (Ramesh Kumar et al. 2023). Both storage options have been already used for decades for the storage of natural

gas and other hydrocarbons worldwide (Foh et al. 1979). The current gas storage system in Germany is designed for storing natural gas. Several interdisciplinary challenges need to be solved to integrate H_2 pore storage facilities into the future energy system.

One significant challenge in the context of H_2 underground storage is the influence of the geological characteristics of saline aquifers on the storage performance, especially recovery efficiency and safety (Heinemann et al. 2021a; Thiagarajan et al. 2022). The selection of suitable sites requires an understanding and evaluation of geological parameters such as rock porosity, permeability and reservoir thickness (Okoroafor et al. 2022; Raza et al. 2022; Malki et al. 2024). The physical properties of H_2 , particularly its high mobility and low density, make secure subsurface storage challenging (Zivar et al. 2021; Jafari Raad et al. 2022).

Dynamic numerical simulations enable the in-depth investigation of reservoir behavior during the injection and withdrawal of H_2 to identify influencing parameters on the storage performance. Ershadnia et al. (2023) conducted a numerical sensitivity study highlighting key geological and operational factors that significantly impact the recovery of H_2 in saline aquifer storage. They conclude that higher permeability anisotropy and lower temperatures increase the extent of H_2 recovery volume while using a cushion gas. Several further sensitivity studies come to the conclusion that permeability is the most influencing factor on upconing (Oldenburg et al. 2024) and storage performance (Okoroafor et al. 2022; Malki et al. 2024). The type of cushion gas can also significantly impact the efficiency and purity of H_2 in an underground storage system (Saeed and Jadhawar 2024a). The presence of cushion gas is crucial to maintaining the operating pressure and achieving the target production volumes (Heinemann et al. 2021b). Various cushion gases were examined in the context of UHS, such as nitrogen (N_2) (Pfeiffer and Bauer 2015; Pfeiffer et al. 2017), carbon dioxide (CO_2) (Wang et al. 2022; Ben Rhouma et al. 2024) and methane (CH_4) (Okoroafor et al. 2022; Izadi Amiri et al. 2024). Among these, CO_2 poses a disadvantage due to its reactivity, particularly its potential to undergo methanation with H_2 (Chai et al. 2023; Izadi Amiri et al. 2024). In contrast, lighter gases as N_2 and CH_4 demonstrate higher H_2 recovery due to reduced viscous fingering and gravity override effects (Kanaani

et al. 2022; Chai et al. 2023; Saeed and Jadhwar 2024a, b; Zhao et al. 2024). Given the consistent evidence supporting the advantages in terms of performance, hydrogen purity, and operational cost (Chai et al. 2023; Zhao et al. 2024; Izadi Amiri et al. 2024), N_2 is selected as the cushion gas in this study.

However, several publications deal with site-specific geological models for numerical simulations of H_2 storage in depleted gas fields (Lysy et al. 2021; Sarı and Çiftçi 2024a, b; Liu et al. 2024) but only a small number on saline aquifers. Wang et al. (2023) analyze the H_2 recovery efficiency of a deep saline aquifer in Wyoming, USA, concluding that H_2 dissolution, as well as relative permeability hysteresis, leads to a reduction of the H_2 recovery. Sainz-Garcia et al. (2017) focus on underground H_2 storage feasibility in Spain's San Pedro belt, emphasizing the importance of detailed geological data for the consideration of seasonal storage. However, the study of H_2 storage in saline aquifers is still in its early stages, and the effects of such storage remain poorly understood, requiring further investigation.

In this study, a numerical sensitivity analysis is conducted to evaluate the impact of uncertainties in critical geological parameters and fluid-rock properties on the performance of a hydrogen storage system, a gap that, to the authors' best knowledge, is not yet addressed in the existing literature. The key novelty of this research lies in its use of a realistic geological reservoir model of a deep saline aquifer at the Ketzin site in Germany, a location currently being investigated as a potential hydrogen storage site. Unlike most prior studies that rely on generic reservoir models with arbitrarily selected geological parameters, this work employs site-specific parameters based on field measurements and experimental data to provide more accurate and applicable insights. The results are systematically analyzed using both existing and newly developed metrics to quantify hydrogen storage performance, to identify the most influencing parameters for future hydrogen storage projects.

2 The Ketzin storage site

The geological structure for storing the injected gas is the Ketzin anticline. It is located at the eastern part of the double anticline structure Ketzin-Roskow in the northeast German Basin (NEGB) as part of the

Central European Basin System (Förster et al. 2006). The structure was formed by salt diapirism, which lifted the overlying Triassic rock formations including Buntsandstein, Muschelkalk as well as Keuper and Lower Jurassic formations. The resulting anticline has a strike of north-northeast-south-southwest and the flanks gently dip at an angle of about 15° (Förster et al. 2006). Based on a 3D survey of 2005 a west-southwest–east-northeast– to east–west–trending Central graben fault zone (CGFZ) was mapped at the top of the anticline. The site was used for gas storage over several decades. In the 1960s, it was used for town gas storage in the shallow Lower Jurassic formations, converted to natural gas storage in 1992 (Beer and Hurtig 1999). In 2004, it became the site of Europe's first onshore CO_2 storage project, with CO_2 injected into the deeper Triassic Stuttgart Formation in the flank of the anticline. During the regular injection phase of several European and national funded projects (e.g., CO_2 SINK, CO_2 MAN, COMPLETE), 67,000 t of CO_2 was injected and permanently stored. The storage facility was dismantled after the projects were completed. From 2022–2023, the HyExpert project H2VL conducted a pre-feasibility study for establishing a H_2 valley in the surrounding region. The study recommends a demonstration project for hydrogen underground storage in a saline aquifer (Wasike-Schalling et al. 2023). Due to the history of the Ketzin site and the availability of geological and experimental data, this site is being used as part of the Helmholtz GEOZeit project to investigate the storage of hydrogen in saline aquifers using laboratory work and numerical simulation (Febbo et al. 2025; Schmidt-Hattenberger et al. 2024; Eckel et al. 2025a).

3 Simulation model description

3.1 Geological model

The conceptual model of the H_2 underground storage at the Ketzin site used in this study is illustrated in Fig. 1. A single well for injection and production is positioned at the top of the anticline, 2 km north of the former CO_2 injection site (Fig. 1), targeting the Stuttgart Formation, which is used as a storage reservoir (Fig. 2). The well has a diameter of 0.3 m and is perforated across the entire thickness of the reservoir (70 m). H_2 is used as a working gas, and N_2

Fig. 1 Illustration of the conceptual model of the potential underground hydrogen storage project showing the former pilot CO₂ storage site in Ketzin with surface facilities, injection well “Ktzi 201” and observation wells “Ktzi 200” and “Ktzi 202” as well as “P300” (modified after Liebscher et al. (2013) and Martens et al. (2012))

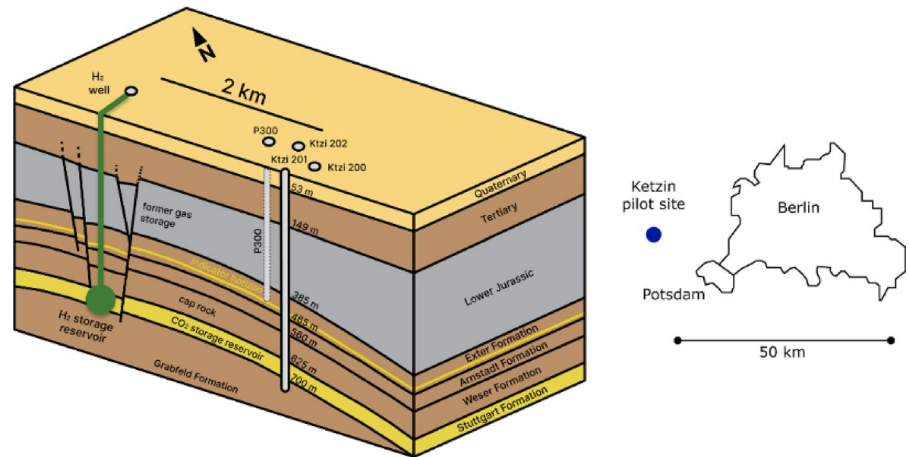
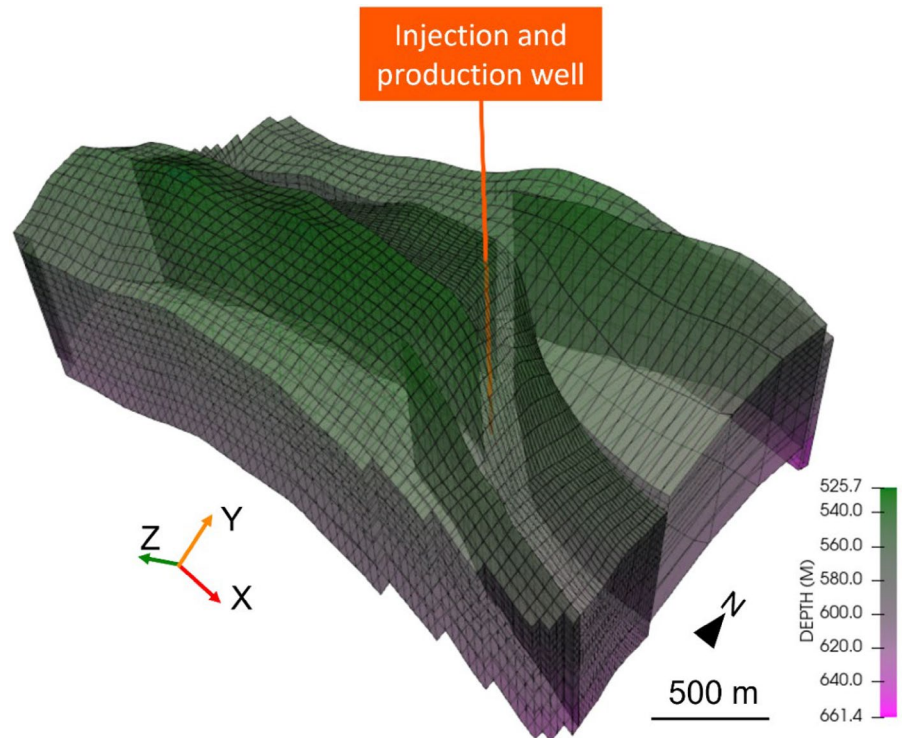


Fig. 2 Oblique view of the 3D numerical grid of the Stuttgart Formation of the Ketzin anticline, including five faults. Depicted is the cell depth. The vertical z-direction is magnified tenfold times



as a cushion gas to displace the formation brine and to build up pressure around the wellbore. The latest static geological model from the CO₂SINK project is implemented (Norden and Frykman 2013), which has a size of approximately 3000 m×2500 m and a total thickness of around 85 m (Fig. 2). The simulation domain includes the storage formation with a thickness of approx. 70 m in depth from 536 to 661 m, which is overlain by a caprock with a thickness of

around 15 m. This depth range aligns with a previous study indicating suitable reservoir conditions for H₂ storage (Okoroafor et al. 2022). The model includes five faults intersecting the area through both caprock and storage reservoir. Two faults are south of the selected well location. The southernmost fault is approx. 500 m from the well, the second 230 m. A lateral separation of approx. 130 m exists between the two northern faults close to the well. The unstructured

grid of the reservoir model consists of 22,040 cells, with 58 cells in the x - and 38 in the y -horizontal direction. The reservoir is divided into 10 cells in the vertical direction (z -direction). The upper two cells have a cell vertical spacing of 5 m, which later will be defined as the caprock. Whereas the cells 3–10 of the reservoir have vertical sizes between 5 m, at the top and 21 m at the bottom of the reservoir. Near the well and between the faults the grid is refined.

3.2 Model conditions

The top two layers of the grid are defined as impermeable caprock layers and the rest as the geological reservoir. Below the caprock and the storage formation, no-flow boundary conditions are implemented. Based on the large horizontal extent of the storage formation, and to prevent an unrealistic increase in pressure due to water displacement, the reservoir is laterally infinite. For the purpose of the sensitivity analysis to test and isolate the influence of different parameters on the reservoir performance, the reservoir lithology is simplified and homogeneously parameterized with porosity ϕ and permeability k . In addition, geomechanical and geochemical aspects are therefore not considered to focus on the effects on the hydrodynamics. All faults are defined to be impermeable in the simulation model. Based on logging data from the Ktzi 200 observation well (Loizzo et al. 2013), an average temperature across the thickness of the formation of $T=33\text{ }^{\circ}\text{C}$ is assumed for the isothermal simulation. A hydrostatic pressure gradient of 40 bar at 400 m is defined. The timesteps during the operational phases (B–D) (see Fig. 4) range from 2 to 300 days. The initial water saturation of all active cells is 1.0.

3.3 Energy storage cycles

The injection and production protocols for phase and cycle lengths of H_2 storage follow the ones defined by Pfeiffer and Bauer (2015), where the demand for energy storage is assumed to be one week to cover shortages in energy production due to natural fluctuations of renewable energies. Before the actual storage operation begins, a one-year-long period (phase A) is simulated to ensure steady-state conditions. This period can be also considered for baseline measurements during the construction of

a demonstrator storage site (see Fig. 4). The storage operation is divided into three phases. First, N_2 is injected for approx. 2 years (710 days, phase B). This phase is followed by the initial H_2 injection phase lasting for 210 days (phase C). Following that, six discharge and charge cycles with shut-in periods are performed (phase D): first 7 days of production, followed by shut-in (5.25 days), then injection for 60 days and 30 days of shut-in.

The bottom hole injection and production pressures (BHP) are limited to 83 bar and 48 bar, respectively. These assumptions are based on the wellbore bottom-hole pressure limit of 83 bar that was set during a former CO_2 injection experiment at a similar depth for the Ketzin site (Liescher et al. 2013). The production pressure is set to 48 bar based on the maximum pressure difference between injection and production of 35 bar (Pfeiffer and Bauer 2015).

3.4 Reservoir simulation software

For this work, the open-source reservoir simulation software MUFITS (Afanasyev 2023) is used for modeling the dynamic energy storage process in the subsurface. MUFITS has been successfully used in a validation study of CO_2 storage benchmarks and history-matched models of the Ketzin site (Afanasyev et al. 2016). In a comparative study with the commercial software CMG GEM, the results showed good agreement in parameters such as plume spread and BHP (Eckel et al. 2025b). The software uses the finite-difference method, 2-phase fluid flow (Darcy's law) and the equation of state (EoS) module COMPS, to model multicomponent gas transport in a saline aquifer (Afanasyev and Vedeneva 2021). The phase behaviour of gas and liquid is implemented by the EoS from Sørense and Whitson (1992), which is a modified version of the Peng-Robinson EoS (Peng and Robinson 1976). Various modifications are included in this EoS, to simulate the phase equilibria of the brine (water and sodium chloride) and the gas components H_2 and N_2 (Afanasyev and Vedeneva 2021). Further details on the modifications to the EoS, the applied binary interaction coefficients, estimations of the brine densities and other fluid properties can be found in Afanasyev and Vedeneva (2021).

4 Sensitivity study concept

4.1 Cases of sensitivity study

To address the impact of various sensitivity parameters on the reservoir storage performance, a base case is perturbed to obtain 10 additional sensitivity scenarios. To isolate and understand their specific effects each sensitivity parameter is assessed individually while keeping all other variables constant. The sensitivity parameters for the reservoir's host rock include variations in porosity and permeability. The salinity of the formation fluid is varied, while the capillary pressure and relative permeability curves are modified to study rock-fluid interactions. To account for low and high dispersivity, the mechanical dispersion coefficient is adjusted. All parameters are constrained within their known ranges for the Stuttgart storage formation based on former dynamic reservoir simulation studies as described below (Table 1).

The porosity of the Stuttgart Formation is reported to vary between $\phi = 0.05$ – 0.35 (Norden and Förster 2010; Förster et al. 2010). These values are based on the lithological and petrophysical core-log interpretation of the CO2SINK project including measurements of helium porosity. This variability is represented in the sensitivity study by two cases: Case 1 (in the following referred to as “Poro min”) and case 2 (“Poro max”). The base case, defined with $\phi = 0.2$, represents the average value between these extremes. Case 3 includes a horizontal permeability value of $k_h=20$ mD (“Perm min” representing flood-plain rocks) from analog outcrop data. This low permeability is caused by a smaller grain size distribution and a larger degree of cementation. Case 4 is representing channels sands, with $k_h= 500$ mD (“Perm max”). The base case is set to an average value of $k_h = 260$ mD between the cases 3 and 4 (Förster et al. 2006). The

anisotropy ratio k_v/k_h is constant for all with a value of 0.3 (Kempka and Kühn 2013). The sensitivity of the brine salinity is assessed by case 5 ($b= 0.5$ mol/kg, “Sal min”) and case 6 ($b = 6.5$ mol/kg, “Sal max”) and the corresponding mean value of $b = 3.5$ mol/kg for the base case (Förster et al. 2006).

Due to the sparse data of the relative permeability and capillary pressure curves of H_2 gas (Saeed and Jadhawar 2024b), the experimental data that uses CO_2 as a working gas in the simulation are integrated. Fleury et al. (2013) report capillary pressure and relative permeability curves based on centrifuge experiments with multiple samples from the reservoir section of the Stuttgart Formation as part of the CO2SINK project at Ketzin. The results are shown in Fig. 3. The influence of a relative permeability curve together with a capillary pressure curve that are shifted towards smaller water saturations (depicted in faint purple color in Fig. 3) and vice versa (dark purple color in Fig. 3) is covered by case 7 (“Cap min”) and 8 (“Cap max”), respectively. Hysteresis effects are discarded, since no capillary pressure hysteresis or relative permeability hysteresis were observed in the experiments with the sandstone samples.

Although a homogenous reservoir is considered, reservoir rocks are inherently heterogeneous, exhibiting variations in petrophysical properties such as permeability, porosity and grain size distribution. To account for the macroscopic effect of physical heterogeneity on the mixing of fluids as they migrate through the rock, the mechanical dispersivity is adjusted in the longitudinal and transverse direction (Feldmann et al. 2016; Pfeiffer et al. 2017). The range implemented in this study is based on the report of the European HyUSPre project (Michelsen et al. 2023). In case 9 (“Dis min”), a grain-scale dispersivity of $\alpha = 3.10e-4$ m is used which is based on core flooding experiments of Berea sandstone (Yang et al.

Table 1 Values of the base case and the low and high value cases of the sensitivity parameters cases

Geological Parameter	Low-value cases	Base case	High-value cases
Porosity ϕ [-]	Case 1: 0.05	0.20	Case 2: 0.35
Horizontal Permeability k_h [mD]	Case 3: 20.00	260.00	Case 4: 500.00
Salinity b [mol/kg]	Case 5: 0.50	3.50	Case 6: 6.50
Capillary Pressure p_c [bar] and relative permeability k_r [-]	Cases 7 and 8 and corresponding base case are defined in Fig. 3		
Dispersivity α [m]	Case 9: $3.1e-4$	<i>neglected</i>	Case 10: 25.00

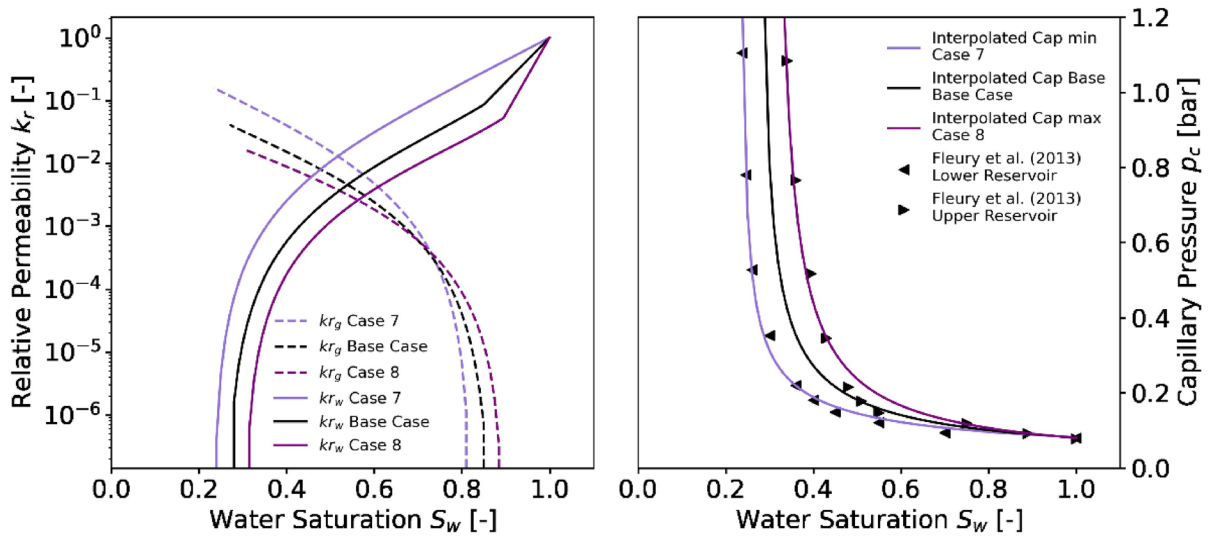


Fig. 3 Drainage and imbibition gas–water capillary pressure (p_c) and relative permeability (k_r) curves based on (Fleury et al. 2013). A linear curve fitting of the data points of (Fleury et al. 2013) is applied and the faint purple curve and the dark purple curve are applied in cases 7 (“Cap min”) and 8 (“Cap

max”), respectively. A mean curve for the relative permeability and the capillary pressure is extracted by applying linear interpolation on the two existing curves. These are used for base case scenario

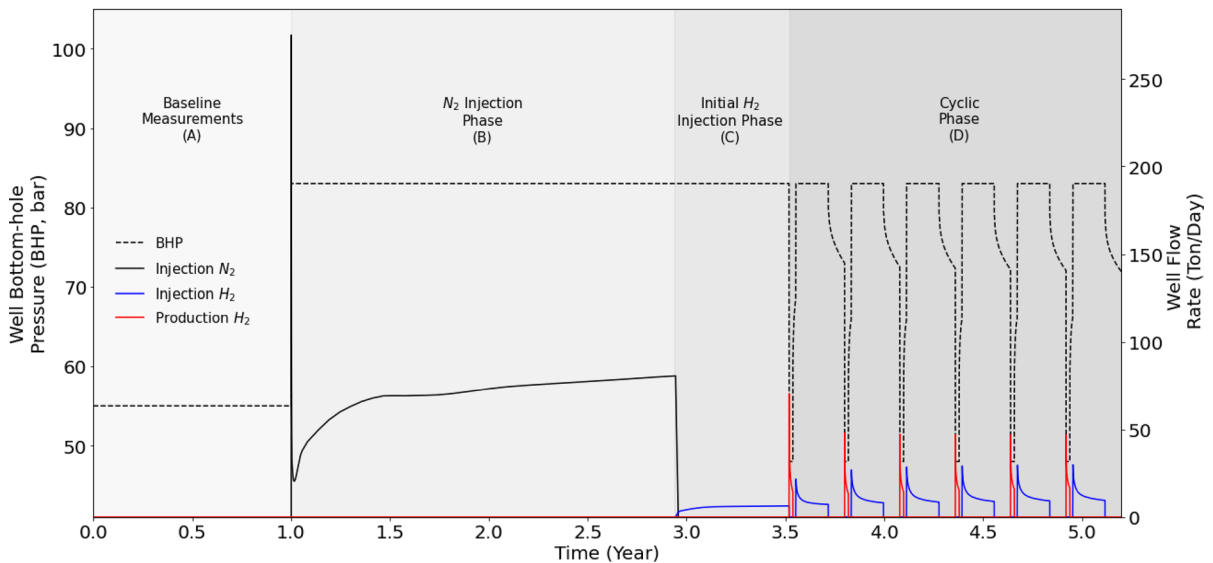


Fig. 4 Base case flow simulation results at wellbore bottom-hole conditions. The storage is realised in three phases: **A** baseline measurements, **B** N_2 injection, **C** initial H_2 injection and **D** cyclic injection and production phases

2023). Case 10 (“Dis max”) adopts a larger field-scale value of $\alpha = 25$ m, based on observations from a field study utilizing H_2 as a tracer in a porous reservoir (Laille et al. 1986). The dispersivities are assumed to

be phase independent. The base case focuses on the core aspects of plume expansion without considering diffusion and dispersion between fluids and gas components.

4.2 Assessment parameters

To quantify the influence of the sensitivity parameters, gas rates and total gas masses of injection and production cycles are analyzed. To evaluate the productivity and sustainability of the storage process, the following assessment parameters are studied and compared. To quantify how much cushion gas in relation to working gas is withdrawn during the production process, the total gas mass ratio Q_i of produced H_2 to N_2 during each cycle i is analyzed:

$$Q_i = \frac{M_{totalH_{2,i}}}{M_{totalN_{2,i}}} \quad (1)$$

In addition, a productivity index (PI) is defined by the H_2 mass produced over a specified time period (M_{Prod}/t_{Prod}) divided by the difference between the squared reservoir pressure (p_{Res}) and squared production pressure (p_{Prod}) (Okoroafor et al. 2022):

$$PI = \frac{M_{Prod}/t_{Prod}}{(p_{Res}^2 - p_{Prod}^2)} \quad (2)$$

Here, the period corresponding to the energy cycles is considered (from the first to the sixth cycle). A sustainability index SI is defined to relate the productivity index to the total amount of injected H_2 , calculated by dividing the former by its injectivity counterpart:

$$SI = \frac{\frac{M_{Prod}/t_{Prod}}{(p_{Res}^2 - p_{Prod}^2)}}{\frac{M_{Inj}/t_{Inj}}{(p_{Inj}^2 - p_{Res}^2)}} \quad (3)$$

M_{Inj} is the injected cumulative H_2 , t_{Inj} is the injection time and p_{Inj} the pressures of injection.

5 Results

5.1 Base case

The evolution of BHP as well as H_2 and N_2 well flow rates as a function of time during the four phases ((A) baseline measurements, (B) N_2 injection, (C) initial H_2 injection and (D) cyclic injection and production phase) of the base case scenario is

shown in Fig. 4. It shows that the set injection and production pressures are achieved and kept constant for the duration of each operation phase (i.e., storage and withdrawal). During well-stop, the BHP decreases after each injection phase and increases after each production phase. As the well is opened for N_2 injection in phase B, a significant pressure difference causes a large amount of gas to enter, resulting in a rapid increase of the injection rate up to 280 t/day (Fig. 4). This is due to a substantial rise in gas density and a localized build-up of pore pressure. This, in turn, leads to a sudden drop in the gas injection rate to 20 t/day. As the gas starts to displace the brine to adjacent pore spaces, the gas injection rate slowly increases and attains 80 t/day at the end of phase B.

During phase B, a total amount of 50,142 t of N_2 is injected. Figure 5 displays the total production of H_2 , N_2 and brine mass over time as well as the withdrawal rates during the production time of the first and last cycle. During the initial H_2 injection in phase C, the injection rate reaches a nearly constant value of 6 t/day and overall, 1200 t of H_2 are injected during that period. Despite the same BHP during injection, the total H_2 mass is significantly lower than the N_2 injection mass due to the lower molecular weight and compressibility of H_2 (Kanaani et al. 2022). This is followed by the cyclic operation in phase D with a peak in the well flow rate at the onset of each production phase. This peak quickly reduces as the difference between the initial BHP production pressure (48 bar) and the reservoir pressure around the well (around 80 bar) diminishes.

Over the six storage cycles, the production rates of H_2 increase from 14.5 to 16.4 t/day, compared to the last step of each cycle, while that of N_2 decreases from 12.8 to 1.8 t/day due to its displacement by H_2 around the well. This is in agreement with other studies that report increasing production rates with increasing cycle number (Pfeiffer and Bauer 2015; Feldmann et al. 2016; Sainz-Garcia et al. 2017). In total, 898 t of H_2 , 154 t of N_2 and 96 t of brine are produced, with brine production decreasing over time.

Similar effects are observed in the subsequent injection phases, with an initial peak in the gas flow rate followed by a leveling off (Fig. 4). The H_2 injection rate increases from 7 t/day (first cycle, last time step) to 9.5 t/day (6th cycle) (Fig. 4).

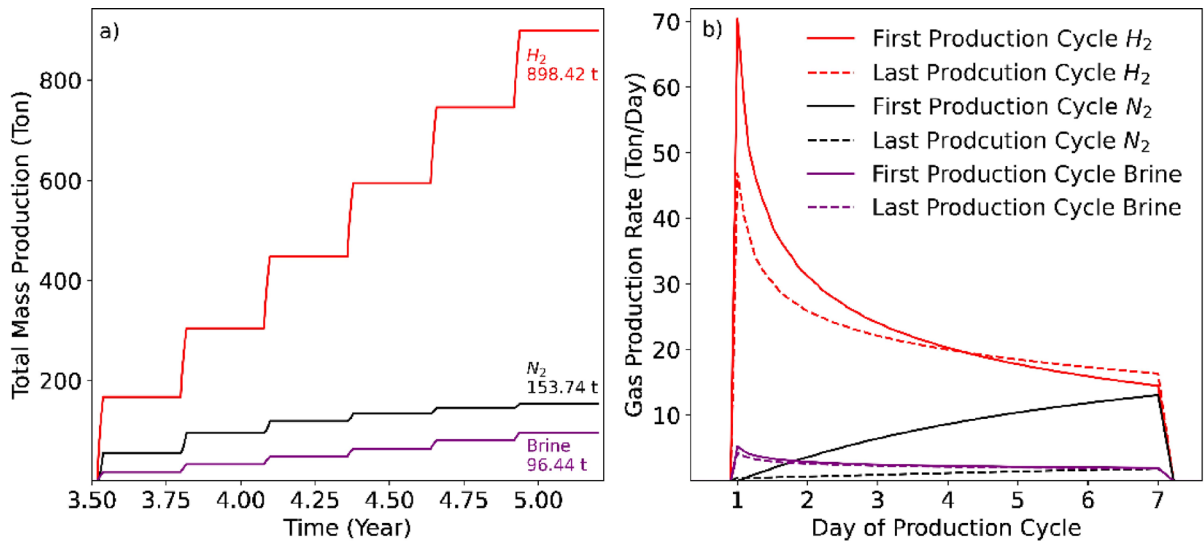


Fig. 5 Total mass produced as a function of time **a** and production rates during the first and last cycle for H₂, N₂ and brine **b** in the base case scenario

Figure 6 shows snapshots of the extent of gas saturation in the reservoir and H₂ gas mass fraction in the uppermost reservoir layer at various times. During the N₂ injection, the injected gas spreads in the lateral direction and accumulates right beneath the caprock due to the large density difference between gas and brine. This is illustrated in the bottom snapshot Fig. 6 which shows the gas saturation in a vertical section. Since the injection well is perforated through the complete depth of the reservoir, the gas saturation close to the well is the highest, i.e., around $S_g = 0.50$ – 0.60 . The H₂ gas mass fraction near the well is $\omega_{H_2} = 0.57$ after the first and $\omega_{H_2} = 0.92$ after the last production cycle (Table 2). With the onset of the H₂ injection, N₂ near the well is displaced and the highest H₂ mass fraction is located right around the injection point (see Fig. 6 middle panel). The gas plume extends to and beyond the opening of the northern fault. At the end of the simulation, the maximal W-E and N-S extent is approximately 950 m, using a gas saturation threshold of $S_g = 0.20$.

5.2 Sensitivity cases

The sensitivity of the geological parameters is studied in terms of several performance parameters. These include the production rates during the first and last cycle (Fig. 7) as well as the amount of injected and

produced H₂, N₂ and brine (Fig. 8), the hydrogen gas mass fraction around the well, gas saturation and plume extent (Fig. 9 and Table 2). Furthermore, two derived assessment parameters are studied: hydrogen mass ratio (Sect. 5.2.6) as well as productivity and sustainability indices (Sect. 5.2.7).

5.2.1 Porosity (Case 1 and 2)

The decrease in porosity, leads to a reduction in available pore space, resulting in a higher gas saturation ($S_g = 0.70$) around the wellbore in the uppermost reservoir layer compared to the base case ($S_g = 0.64$, Table 2). This positively affects N₂ and H₂ injection by increasing gas relative permeability around the wellbore. Comparing the total injected masses of N₂ and H₂ for cases 1 and 2 (Fig. 8a versus b) against the base case scenario, 20% more N₂ and 54% more H₂ can be injected, while the high porosity case results in injecting 6% and 9% less of that, respectively. In contrast, the H₂ total production mass varies less between the base case (898 t), the low (944 t, +5%) and the high porosity cases (838 t, -7%) (Fig. 8d). This can also be seen in Fig. 7b showing the H₂ production rates at the last timestep of the cycles. Here, the high porosity case (13–16 t/day) and the low case (18–17 t/day) differ only slightly from each other. The amount of N₂ produced also shows only minor

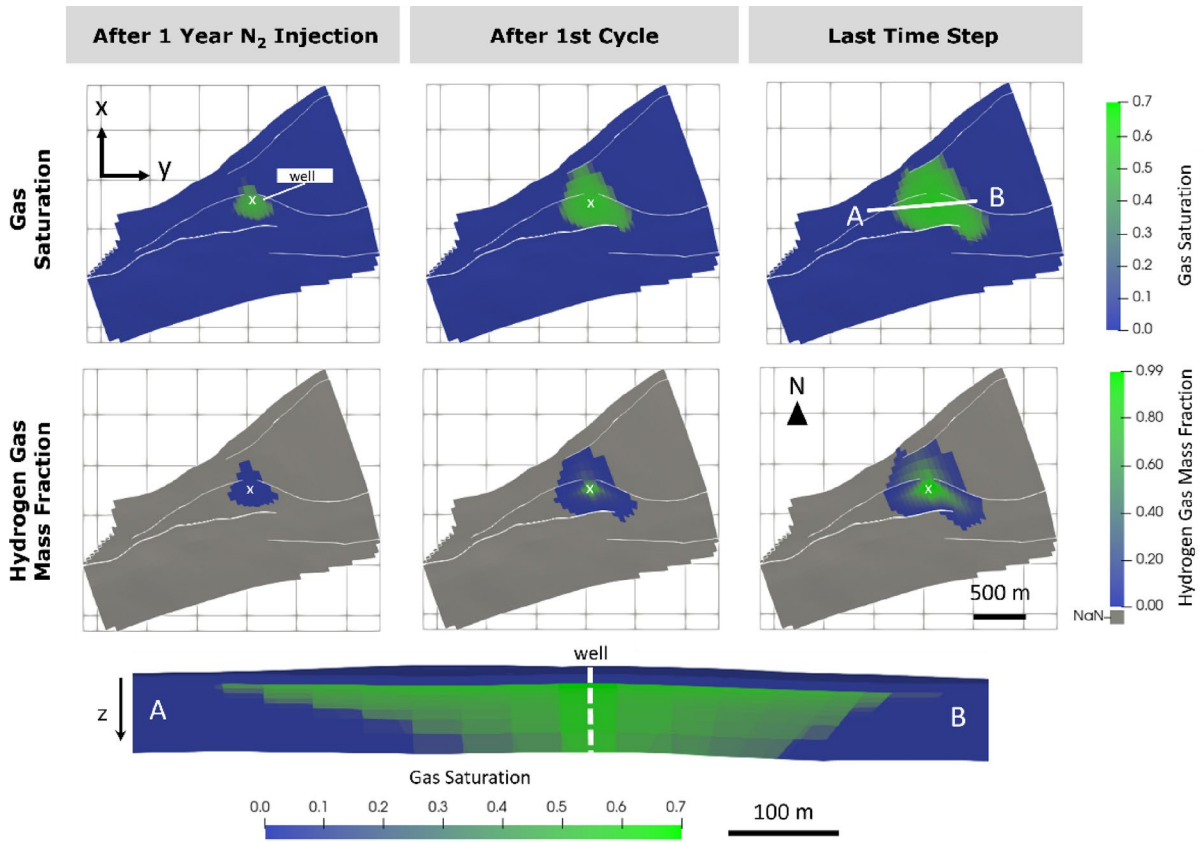


Fig. 6 Top view of gas saturation (top panel) and H₂ gas mass concentration (middle panel) of the base case at the top reservoir layer after one year of N₂ injection, after the first cycle and at the last time step. The faults are shown in white. A gas frac-

tion of 0 is indicated by NaN in grey. The bottom figure shows the gas saturation step in a vertical section with endpoints A–B at the last time step

Table 2 Hydrogen gas mass fraction at the well after the first and last production cycle, the distribution of H₂ ($\omega_{H_2} = 0.2$) in x- and y-direction and the gas saturation near the well of all cases at the top reservoir layer

	Hydrogen gas mass fraction ω_{H_2} [-]		Extent of plume spreading [m]		Maximum gas saturation S_g [-]
	at the well		at $\omega_{H_2} = 0.2$		at the well
	after 1st production cycle	after 6th production cycle	W-E (x-direction)	N-S (y-direction)	after last time step
Base case	0.57	0.92	950	950	0.64
Case1: Poro min	0.68	0.91	2200	1800	0.70
Case 2: Poro max	0.54	0.93	650	710	0.61
Case 3: Perm min	0.29	0.81	200	120	0.44
Case 4: Perm max	0.59	0.91	1400	1300	0.67
Case 5: Sal min	0.60	0.93	1100	1000	0.65
Case 6: Sal max	0.52	0.91	780	800	0.56
Case 7: Cap min	0.50	0.86	1400	1600	0.71
Case 8: Cap max	0.60	0.96	740	640	0.59
Case 9: Dis min	0.57	0.92	900	960	0.64
Case 10: Dis max	0.36	0.63	500	530	0.47

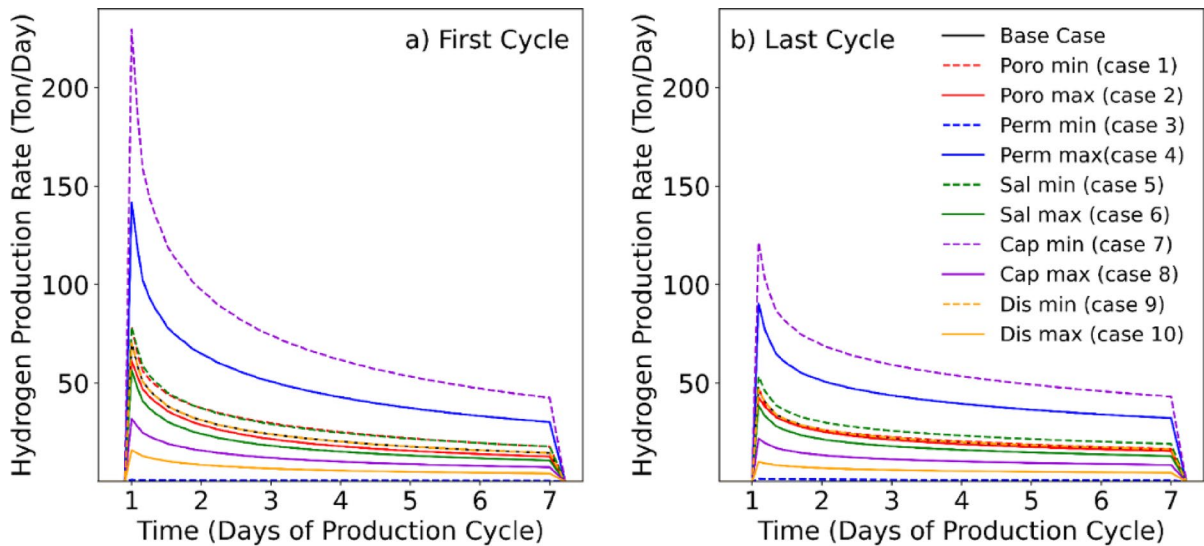


Fig. 7 H₂ production rates as a function of time during **a** the first and **b** the last production cycle

changes compared to the base case with -6.6% in the low case and $+1.1\%$ high case scenario (Fig. 8c). The total mass of brine produced, on the other hand, differs significantly from the base case (Fig. 8e). The low porosity case produced the least brine during the whole simulation period out of all cases (22.5 t, -77%). In contrast, the high porosity case produced 68% more brine than the base case. Due to the smaller pore space but higher gas masses in the low porosity case, the gas migrates further in all directions, as shown in the snapshots in Fig. 9 and Table 2 ($x=2220$ m, $y=1800$ m). Our results confirm the trend identified by Malki et al. (2024) that in saline aquifers with higher porosity, the H₂ injection volume tends to decrease, while brine production increases. However, consistent with their findings, we find that storage performance is more sensitive to variations in other geological parameters, such as permeability.

5.2.2 Absolute permeability (Case 3 and 4)

The low permeability case (case 3) shows the lowest total injected mass of N₂ (2295 t) and H₂ (258 t, see Fig. 8a and b) among all scenarios. Accordingly, the high permeability case (case 4) ranks second highest in total injected N₂ (103,500 t) and H₂ (11,600 t).

The low permeability case results in the lowest total mass produced, with 32 t of N₂ and 30 t of H₂ (Fig. 8c and d) and H₂ production rates are

nearly negligible with <0.7 t/day (Fig. 7b). In contrast, the total production of the high permeability case increases significantly to 314 t N₂ and 1780 t H₂ ($+105\%$ and $+99\%$ compared to the base case). Brine production is 31% lower in the low permeability case compared to the base case, whereas it is close to the base case value in the high permeability case (Fig. 8e).

Variations in reservoir permeability strongly influence the simulation results. Increased absolute permeability accelerates the fluid flow through the reservoir, leading to increased injection and production rates compared to the base case scenario. This is also shown by the larger lateral spread of the gas plume ($x=1400$ m, $y=1300$ m, Fig. 9 and Table 2) while maintaining high gas saturation near the well ($S_g = 0.67$). On the other hand, lower permeability increases flow resistance, resulting in lower gas saturations ($S_g = 0.44$) and a smaller plume size ($x=200$ m, $y=120$ m) (Table 2), leading to significantly reduced injection and production rates. The same trend in increasing the injection volumes by increasing the permeability could be shown by Malki et al. (2024) and Heinemann et al. (2021b).

5.2.3 Salinity (Case 5 and 6)

Increased salinity leads to lower total injection of N₂ (36,100 t, -28%) and H₂ (3800 t, -27%) while

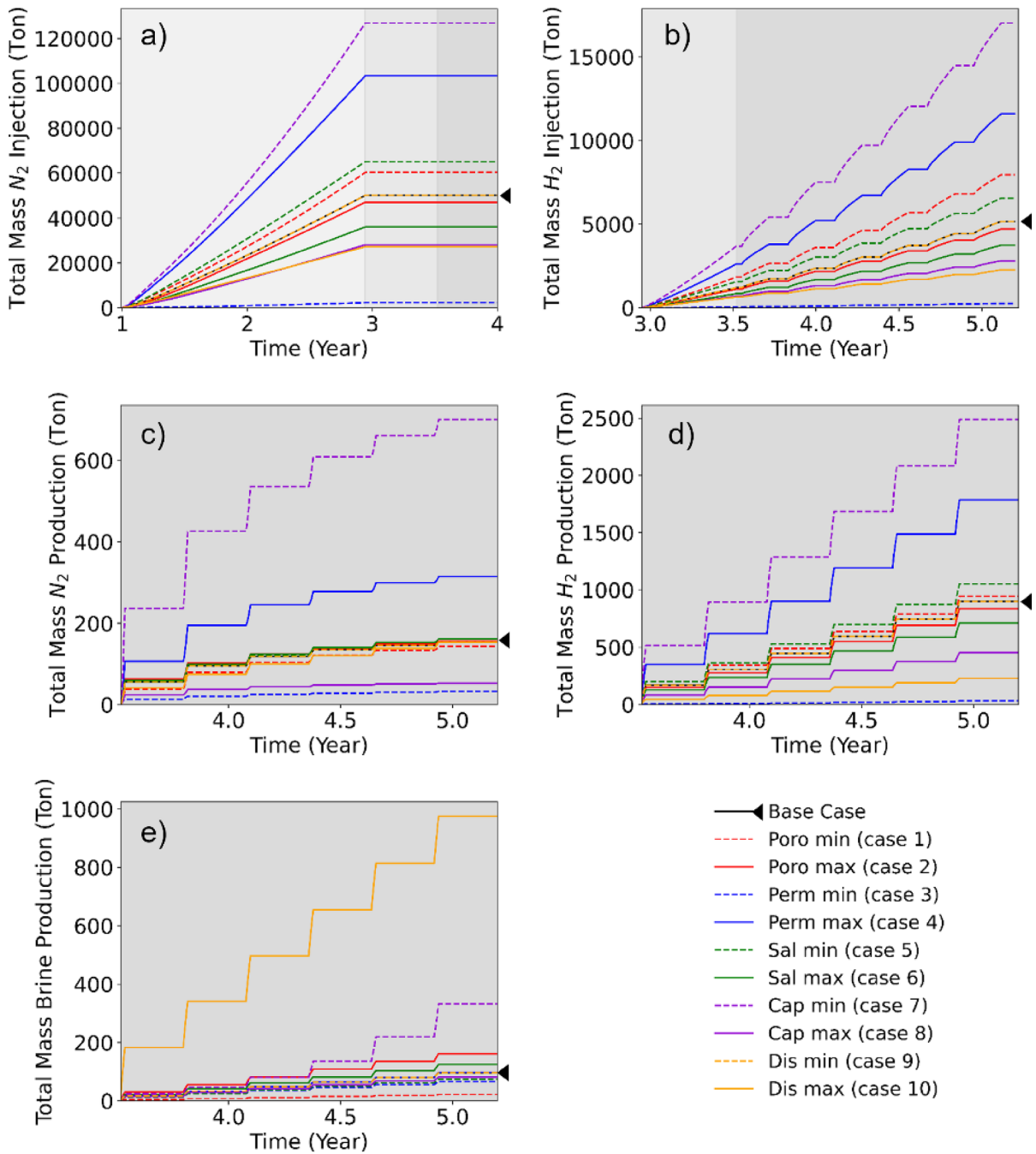


Fig. 8 Total mass injection of **a** cushion gas N_2 and **b** H_2 , **c** total mass production of N_2 , **d** H_2 and **e** of brine as a function of time. The operational phases are color-coded according to Fig. 4

decreased salinity results in higher injection of N_2 (65,100 t, +30%) and H_2 (6600 t, +27%, Fig. 8a and b).

Cases 5 and 6 minimally affect N_2 production but increase or decrease H_2 production by approximately 20% compared to the base case (Fig. 8d),

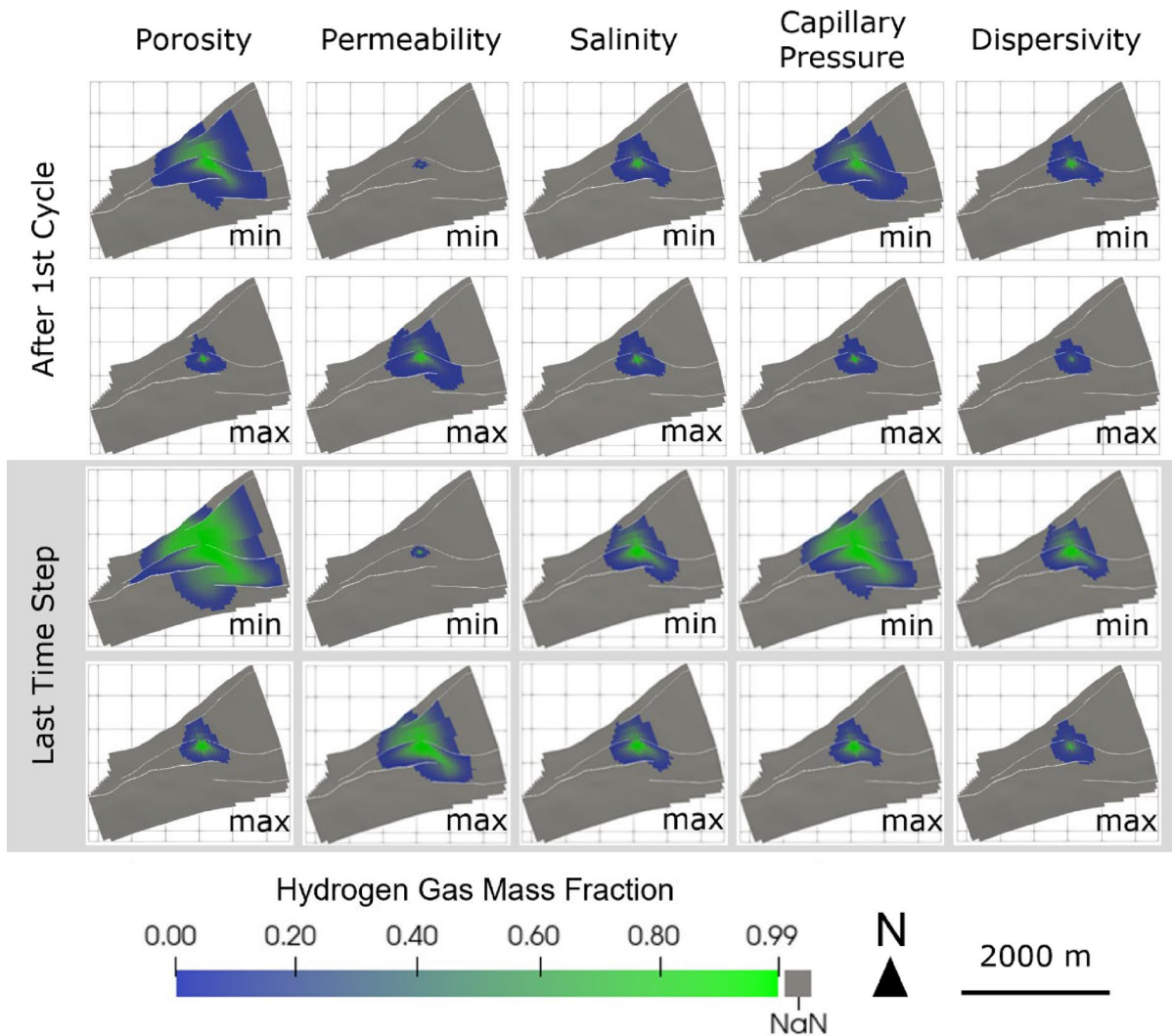


Fig. 9 Top view illustrating the spatial distribution of hydrogen gas mass fraction after the first injection cycle and last timestep at the top reservoir layer; the faults are shown in white. A gas fraction of 0 is indicated by NaN in grey

respectively. In contrast, the brine production is higher and lower (by roughly $\pm 25\%$) in the high and low salinity case, respectively. Changing salinity impacts results significantly through brine dynamic viscosity, which varies from $\mu = 1.071 \times 10^{-3}$ Pa s in the base case, increasing by 49% in high salinity and decreasing by 27% in low salinity cases. An increase in brine viscosity can be translated into an increase in the mobility contrast resulting in a less efficient displacement of the in-situ brine (Heinemann et al. 2021a, b). The mobility contrast is the ratio of mobilities of displacing and displaced fluid (Medina et al. 2024). Therefore, an increase in salinity results in

reduced gas injection rates and this effect is visible in Fig. 9, depicting gas spreading in the x- and y-directions. The lateral plume extent reaches approximately 800 m in the high salinity case and about 1100 m in the low salinity case (Table 2). Additionally, increasing salinity raises brine density by up to 8%, while decreasing salinity lowers it by about 9%. Therefore, despite the increase in brine viscosity and the consequent reduction in its mobility at high salinity, the higher brine density leads to greater brine production in terms of mass, and vice versa. The salinity of the brine also affects the solubility of H_2 . The H_2 solubility decreases with increasing salinity (salting-out

effect), which is consistent with existing analyses (Li et al. 2018; Chabab et al. 2020). However, the molar mass fraction of the aqueous phases is very small and increases/decreases from $4.7e-04$ (base case) to $8.0e-04$ and $2.4e-04$. The recovery of dissolved hydrogen is possible, but it is an economic and technical issue that needs to be discussed in terms of the costs involved.

5.2.4 Capillary pressure and relative permeability (Case 7 and 8)

Changes in capillary pressure and relative permeability curves significantly impact injection and production. Near the borehole, where gas saturations are high ($S_g > 0.5$), case 7 shows better drainage and gas flow due to higher gas relative permeabilities and much lower capillary pressures (see Fig. 3, regime of $S_w < 0.5$). Consequently, the total injected mass of H_2 (17,000 t) and N_2 (127,000 t) in case 7 exceeds the base case by over 230% and 150%, respectively (Fig. 8a and b), which also leads to higher gas saturations around the injection point (Table 3). Improved flow conditions also result in a 245% increase in brine production, which is the second highest value of all cases (Fig. 8e).

Table 3 Hydrogen gas mass fraction near the injector after the first and sixth production cycle, total injected and produced hydrogen mass and percentage deviation from the base case for all cases

	Total injected hydrogen		Total produced hydrogen	
	Mass [t]	Deviation base case [%]	Mass [t]	Deviation base case [%]
Base case	5163.6		898.5	
Poro min	7950.6	+54	944.6	+5
Poro max	4711.6	-9	838.0	-7
Perm min	258.8	-95	29.9	-97
Perm max	11,592.5	+125	1785.5	+99
Sal min	6557.9	+27	1051.5	+17
Sal max	3744.8	-27	711.9	-21
Cap min	17,023.3	+230	2489.1	+177
Cap max	2812.9	-46	452.5	-50
Dis min	5163.1	0	898.4	0
Dis max	2271.4	-56	230.4	-74

Conversely, the high capillary pressure case (case 8) displays approximately 45% lower injection mass for N_2 (28,100 t) and H_2 (2800 t). Similarly, near the borehole, where gas saturation is reduced compared to the base case, there is a notable reduction in both relative gas permeabilities and capillary pressure. This results in a total withdrawal of 52 t of N_2 and 450 t of H_2 , which is 66% and 50% less than the base case, respectively, while the brine production is slightly reduced by 15% (Fig. 8c, d and e).

Figure 9 and Table 2 visualize the large impacts of cases 7 and 8 on the plume expansion: Case 7 exhibits increased plume spread ($x = 1400$, $y = 1600$ m) and higher gas saturation near the borehole ($S_g = 0.71$), whereas case 8 shows reduced plume extent ($x = 740$, $y = 640$ m) and lower gas saturation ($S_g = 0.59$).

5.2.5 Mechanical dispersion (Case 9 and 10)

High mechanical dispersion (case 9) enhances the gas plume spread and mixing of gas with the water phase in the porous rock formation, reducing gas saturation compared to the base case where dispersion is neglected. As indicated in Table 2, the gas saturation at the injection point (at the top reservoir layer) decreases to $S_g = 0.47$ from $S_g = 0.64$ in the base case. Lower gas saturations lead to a decrease in gas relative permeability while increasing water relative permeability. Consequently, gas injection is reduced, resulting in a total injected mass of 27,000 t N_2 and 2300 t of H_2 , corresponding to a reduction of 46% and 56%, respectively. This also affects the W-E and N-S expansion of the gas plume with a much smaller lateral expansion of approximately 500 m. Conversely, brine withdrawal is significantly enhanced, reaching a total produced mass of 980 t, the highest among all cases (+910%). Gas production decreases overall, with N_2 production showing no changes and H_2 production experiencing a larger reduction of 74% compared to the base case.

The low dispersion case (case 9) remains nearly unchanged from the base case in terms of injection and production values since the dispersion length included in the model is much smaller compared to the advective length scale which dominates the transport process.

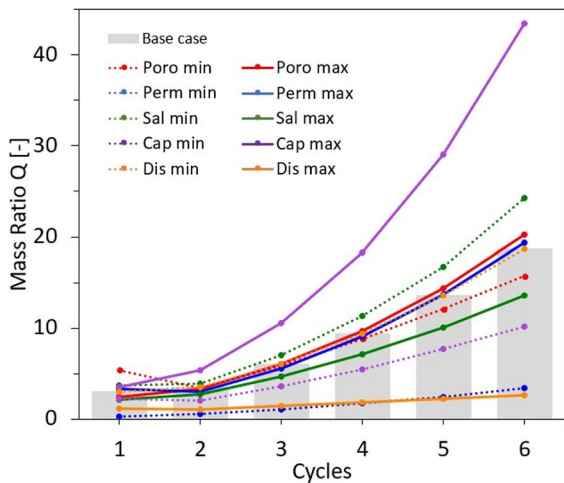


Fig. 10 The ratio of produced H_2 mass over the produced N_2 mass of each cycle (Q) in the function of the cycle number for all simulation cases

5.2.6 Hydrogen mass ratio

For each cycle, Fig. 10 shows the ratio of the produced H_2 mass over the produced N_2 mass (Q) for all 10 cases. This ratio allows to analyze the performance of the cases according to the hydrogen mass ratio of each cycle. In the base case scenario, three times more H_2 mass than N_2 mass is produced in the first cycle. This difference factor increases to 18 by the sixth cycle. All other cases show an improvement in the H_2 to N_2 ratio over successive cycles as well. The growth of increasing Q with time is reflected in Table 3.

Compared to the base case, the most significant improvement in the H_2 to N_2 ratio is seen with increased capillary pressure, with the ratio growing from 3.5 in the first cycle to 43.5 in the sixth cycle. This is followed by the decreased salinity case with a maximum H_2 to N_2 ratio of 24.3 during the sixth cycle. In contrast, the cases with low permeability and high mechanical dispersion have the most negative effects on the ratio, with maximum H_2 to N_2 ratios of 3.4 and 2.7 in the sixth cycle (Fig. 10). However, high permeability does not invariably yield a higher Q and the value of the high permeability case is only slightly above the base case. Similar behavior is observed in the dispersion cases. Strong mechanical dispersion causes increased mixing effects resulting in the production of cushion gas that is similar to

or even exceeds the one of the working gas. A low dispersion coefficient shows similar results to the base case where dispersion effects are ignored. When the porosity is adjusted, there are only minor changes in the H_2 to N_2 ratio compared to the base case scenario. The increased porosity case leads to a slightly higher ratio ($Q = 20.2$), while the reduced case leads to a slightly reduced ratio ($Q = 15.7$) in the last cycle. The increased salinity and reduced capillary pressure cases also show a reduction of the ratio to 13.6 and 10.2 in the last cycle compared to the base case.

All cases with a positive influence on the H_2 to N_2 ratio show higher H_2 gas mass fractions after the production cycles near the well compared to the base case, which increases the mixing of the gases. The negative influencing parameters show low H_2 gas mass fractions due to the small injection masses (see Table 3) and therefore reduced mixing of the gases after the first and sixth production cycles at the top reservoir layer. The H_2 gas mass fraction after the first and last cycle for all scenarios at the top reservoir layer is reflected in Table 3.

5.2.7 Productivity and sustainability index

Figure 11 shows the variation in productivity index PI (defined in Eq. 2 in Sect. 5) and the sustainability index SI (defined in Eq. 3 in Sect. 5) for all modelling scenarios. The base case serves as a reference, with a PI of $354 \text{ Sm}^3/\text{day}/\text{bar}^2$ and SI of 13.9. The presence of SI values greater than 1 can be attributed to the much longer injection phase (60 days) compared to the production phase (7 days). The sensitivity parameters are categorized by comparing them with the base case, into the following groups: (1) $PI > PI_{base}$ and $SI < SI_{base}$, (2) $PI < PI_{base}$ and $SI > SI_{base}$, (3) PI and SI are lower and (4) cases with no significant changes compared to the base case.

Group 1 includes the cases of decreased capillary pressure ($PI = 982 \text{ Sm}^3/\text{day}/\text{bar}^2$, $SI = 10.6$), increased permeability ($PI = 704 \text{ Sm}^3/\text{day}/\text{bar}^2$, $SI = 11.2$), decreased salinity ($PI = 414.6 \text{ Sm}^3/\text{day}/\text{bar}^2$, $SI = 11.7$) and decreased porosity ($PI = 372 \text{ Sm}^3/\text{day}/\text{bar}^2$, $SI = 8.6$), meaning that the production process is more efficient but the overall sustainability is negatively affected. The relation between the relative improvements of injection and production mass compared to the base case is crucial. In group 1, the relative improvement in injection mass is higher than

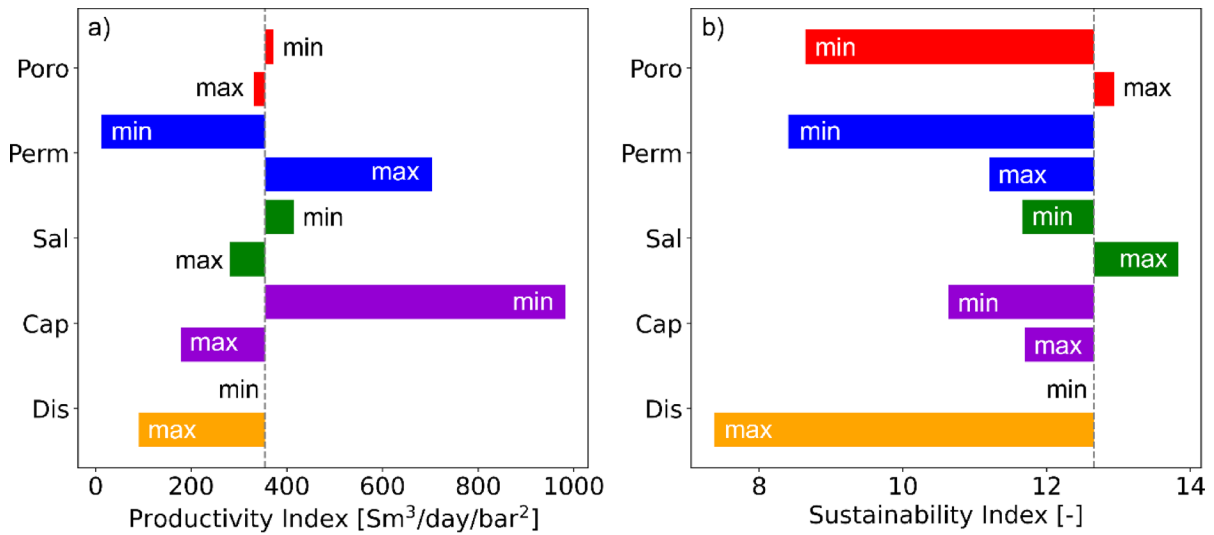


Fig. 11 Tornado plot of **a** Productivity Index (PI) and **b** Sustainability Index (SI) for the cases. The vertical dashed line is a reference and represents the base case values

in production mass. The high permeability scenario shows a 125% increase in injected hydrogen mass compared to the base case, while the production mass shows a lower improvement of 99% (Table 3). The total injected and produced hydrogen of the cases in tons as well as their deviation percentages from the base case is reflected in Table 3.

Increased porosity ($PI = 330 \text{ Sm}^3/\text{day}/\text{bar}^2$, $SI = 12.9$) and increased salinity ($PI = 281 \text{ Sm}^3/\text{day}/\text{bar}^2$, $SI = 13.8$) show a decrease of PI but an improvement of SI (group 2). As an example, in the high salinity case, the injected mass decreases by 27%, while the produced mass decreases by 21% (Table 3).

In group 3, increased capillary pressure ($PI = 178 \text{ Sm}^3/\text{day}/\text{bar}^2$, $SI = 11.7$), high dispersity ($PI = 91$, $SI = 7.4$) and low permeability ($PI = 11.8$, $SI = 8.4$) reduce both PI and SI compared to the base case. This is due to a significant decrease in hydrogen injection and production masses. Due to the low changes in the low dispersity case ($PI = 354$, $SI = 12.7$), this case shows no significant differences (group 4).

Since there are no cases in this sensitivity study improving both PI and SI at the same time, the most promising cases are those in group 2 (increased porosity and salinity) when prioritizing the long-term sustainability of the storage site, while the cases of group 1 (decreased capillary pressure, salinity,

porosity and increased permeability) can maximize the total produced hydrogen mass.

6 Discussion and outlook

The simulation results show that performance parameters are most sensitive to the shape of the relative permeability and capillary pressure curves, as well as permeability. For instance, the total mass of injected and produced cushion and working gas can vary significantly from the base case. Changes in relative permeability and capillary pressure curves can also increase both hydrogen mass ratio and productivity index and accurate measurements of these parameters for the specific reservoir are crucial. Additionally, each parameter significantly affects the maximum lateral spread of injected hydrogen gas along the reservoir top. The plume spread can range from 120 m (low permeability) to 1800 m (low porosity). In the latter cases, the gas plume also penetrates faults. This variation necessitates controlling plume spread with an optimized injection protocol to meet legal storage security requirements and prevent unwanted storage loss (Heinemann et al. 2021a).

The numerical model results face several constraints. The storage formation comprises a high variability of the lithology of assumed fluvial

origin—including parts of sandy string-facies, rocks with good reservoir conditions alternating with muddy floodplain facies and rocks with poor reservoir quality (Förster et al. 2006). This heterogeneity likely affects gas plume distribution and well rates as shown by adjusting the mechanical dispersivity in the model which estimates the impact of the macroscopic effect of physical heterogeneity on the mixing of fluids. Multi-level heterogeneity could also reduce the H₂ fraction in produced gas (Bo et al. 2024). Additionally, the relative permeability and capillary curves of the model do not account for hysteresis, potentially underestimating residual hydrogen trapping and overestimating mobile phase accumulation, produced H₂, and extracted water (Ershadnia et al. 2023). Although geochemical and microbiological processes may lead to hydrogen storage losses in the subsurface (Heinemann et al. 2021a; Thiyagarajan et al. 2022), these are beyond the scope of the present study. Potential storage loss from hydrogen leakage through faults or caprock, cyclic stress fluctuations, and geochemically (clay-swelling) induced stresses are not addressed in this study. Due to limited fault characterization data, the sensitivity study should be extended with plausible hydro-mechanical fault parameters and a geomechanical analysis for caprock integrity and fault stability.

Developing a hydrogen storage demonstrator based on these findings will verify the practicality and efficiency of the proposed strategies and offer insights to optimize and scale hydrogen storage at other sites. This includes designing operational strategies like pressure settings for injection and production, and gas injection rates and durations.

7 Conclusions

In this study, the effect of uncertainty in geological parameters on the performance of a proposed underground hydrogen storage in a deep saline aquifer at a potential, former Ketzin gas storage site in North-East Germany using an open source multicompositional reservoir simulator is investigated. The energy storage system is assumed to be designed for covering energy production shortages due to natural renewable energy fluctuations and to use nitrogen as cushion gas in a single well. The range of each geological parameter is constrained by results and experiences gained during

the CO₂ gas storage. It includes reservoir rock porosity and permeability, brine salinity, relative permeability curves as well as mechanical dispersivity. The efficiency of the storage system is assessed through several parameters.

Based on the results of the numerical assessment, the following conclusions can be made:

- The base case, with average sensitivity parameters of the Stuttgart Formation, shows increasing production masses of H₂ and decreasing N₂ and brine over time as well as increasing H₂ injection masses.
- All scenarios demonstrate an increasing H₂ to N₂ mass ratio over successive cycles. This trend is most notable in the increased capillary pressure case, which shows the highest H₂ to N₂ ratio improvement. It shows the notable role of capillary pressure and relative permeability in affecting gas mixing and gas saturation near the well.
- Scenarios with low absolute permeability and high mechanical dispersion show a significant decrease in the H₂ to N₂ ratio due to increased mixing of H₂ and N₂. These conditions lead to lower H₂ gas mass fractions near the well, demonstrating the negative impact of these parameters on maintaining high hydrogen H₂ to N₂ ratio.
- While low permeability has a strong negative effect on the H₂ to N₂ ratio, productivity and sustainability, high permeability, on the other hand, does not lead to significantly higher gas mass ratios. This infers that there is a limit to the increase in the H₂ to N₂ ratio due to the high gas masses injected.

The results of the present numerical model allow optimizing the operational parameters for the given reservoir characteristics to maximize the performance of the hypothetical underground hydrogen system in a future study. Even though the present study was performed with Ketzin site-specific data, understanding the specific effect of each parameter allows better optimization strategies for porous geological reservoirs with similar characteristics.

Author contributions L. Döpp: conceptualization, validation, data curation, investigation, software, formal analysis, visualization, methodology, writing—original draft, writing—review & editing. A.-M. Eckel: conceptualization, validation, data curation, investigation, software, formal analysis,

methodology, writing—review & editing. M. P. Farkas: conceptualization, investigation, formal analysis, methodology, writing—review & editing. W. Weinzierl: conceptualization, methodology, data curation, software. C. Schmidt-Hattenberger: funding acquisition, conceptualization, writing—review & editing, supervision, project administration. I. Sass: funding acquisition, supervision, project administration.

Funding Open Access funding enabled and organized by Projekt DEAL. The GEOZeit project is funded by the Helmholtz initiative “Geotechnologies for a turnaround in energy supply in Germany”.

Availability of data and material The geological model used in this publication is based on the model provided by Ben Norden from GFZ Helmholtz Centre for Geosciences and is not publicly available at this time. The data will be made publicly available upon future publication. All other cited data are available in the references listed.

Declarations

Competing interests The authors have no competing interests to declare that are relevant to the content of this article.

Open Access This article is licensed under a Creative Commons Attribution 4.0 International License, which permits use, sharing, adaptation, distribution and reproduction in any medium or format, as long as you give appropriate credit to the original author(s) and the source, provide a link to the Creative Commons licence, and indicate if changes were made. The images or other third party material in this article are included in the article’s Creative Commons licence, unless indicated otherwise in a credit line to the material. If material is not included in the article’s Creative Commons licence and your intended use is not permitted by statutory regulation or exceeds the permitted use, you will need to obtain permission directly from the copyright holder. To view a copy of this licence, visit <http://creativecommons.org/licenses/by/4.0/>.

References

- Afanasyev A, Vedeneva E (2021) Compositional modeling of multicomponent gas injection into saline aquifers with the MUFITS simulator. *J Nat Gas Sci Eng* 94:103988. <https://doi.org/10.1016/j.jngse.2021.103988>
- Afanasyev A, Kempka T, Kühn M, Melnik O (2016) Validation of the MUFITS reservoir simulator against standard CO₂ Storage benchmarks and history-matched models of the Ketzin pilot site. *Energy Procedia* 97:395–402. <https://doi.org/10.1016/j.egypro.2016.10.032>
- Afanasyev A (2023) MUFITS reservoir simulation software version 2022.B - Reference manual
- Beer H, Hurtig E (1999) Das geothermische feld in Brandenburg. *Brandenburgische Geowissenschaftliche Beiträge*, pp 57–68
- Ben Rhouma S et al (2024) H₂ storage with CO₂ cushion gas in aquifers: numerical simulations and performance influences in a realistic reservoir model. *Int J Hydrog Energy* 110:101–114. <https://doi.org/10.1016/j.ijhydene.2025.01.423>
- Bo Z et al (2024) Effects of geological heterogeneity on gas mixing during underground hydrogen storage (UHS) in braided-fluvial reservoirs. *Fuel* 357:129949. <https://doi.org/10.1016/j.fuel.2023.129949>
- Chabab S et al (2020) Measurements and predictive models of high-pressure H₂ solubility in brine (H₂O+NaCl) for underground hydrogen storage application. *Int J Hydrog Energy* 45:32206–32220. <https://doi.org/10.1016/j.ijhydene.2020.08.192>
- Chai M, Chen Z, Nourozieh H, Yang M (2023) Numerical simulation of large-scale seasonal hydrogen storage in an anticline aquifer: a case study capturing hydrogen interactions and cushion gas injection. *Appl Energy* 334:120655. <https://doi.org/10.1016/j.apenergy.2023.120655>
- Eckel A-M et al (2025a) Impact of wellbore trajectory and fault transmissibility on underground hydrogen storage in a Saline Aquifer of Ketzin, North German Basin. *J Energy Storage* (In press)
- Eckel A-M et al (2025b) Comparative study of reservoir simulation tools with application of hydrogen underground storage at the Ketzin Site. In: Yao J, Yang Y, Wang W et al (eds) *Progress and challenge of porous media: proceedings of the 16th annual meeting conference on porous media*. Springer Nature Singapore, Singapore, pp 600–612
- Ershadnia R et al (2023) Impact of geological and operational conditions on underground hydrogen storage. *Int J Hydrog Energy* 48:1450–1471. <https://doi.org/10.1016/j.ijhydene.2022.09.208>
- Febbo MB et al (2025) The upper triassic caprock of the ketzin CO₂ storage site, North German Basin: implications for geological hydrogen storage. *Geo Sci Eng* 253:213987. <https://doi.org/10.1016/j.geoen.2025.213987>
- Federal Ministry for Economic Affairs and Climate Action (BMWK) (2020) *The national hydrogen strategy*. Berlin
- Feldmann F, Hagemann B, Ganzer L, Panfilov M (2016) Numerical simulation of hydrodynamic and gas mixing processes in underground hydrogen storages. *Environ Earth Sci* 75:1165. <https://doi.org/10.1007/s12665-016-5948-z>
- Fleury M et al (2013) Advanced and integrated petrophysical characterization for CO₂ storage: application to the Ketzin site. *OGST* 68:557–576. <https://doi.org/10.2516/ogst/2012084>
- Foh S, Novil M, Rockar E, Randolph P (1979) *Underground hydrogen storage. Final report*
- Förster A et al (2006) Baseline characterization of the CO₂SINK geological storage site at Ketzin, Germany. *Environ Geosci* 13:145–161. <https://doi.org/10.1306/eg.02080605016>
- Förster A et al (2010) Reservoir characterization of a CO₂ storage aquifer: the upper Triassic Stuttgart formation in the Northeast German Basin. *Mar Pet Geol* 27:2156–2172. <https://doi.org/10.1016/j.marpetgeo.2010.07.010>

- German Federal Government (2019) Federal Climate Change Act (Bundes-Klimaschutzgesetz)
- Heinemann N et al (2021a) Enabling large-scale hydrogen storage in porous media—the scientific challenges. *Energy Environ Sci* 14:853–864. <https://doi.org/10.1039/D0EE03536J>
- Heinemann N et al (2021b) Hydrogen storage in saline aquifers: the role of cushion gas for injection and production. *Int J Hydrog Energy* 46:39284–39296. <https://doi.org/10.1016/j.ijhydene.2021.09.174>
- Izadi Amiri I, Zivar D, Ayatollahi S, Mahani H (2024) The effect of gas solubility on the selection of cushion gas for underground hydrogen storage in aquifers. *J Energy Storage* 80:110264. <https://doi.org/10.1016/j.est.2023.110264>
- Jafari Raad SM, Leonenko Y, Hassanzadeh H (2022) Hydrogen storage in saline aquifers: opportunities and challenges. *Renew Sustain Energy Rev* 168:112846. <https://doi.org/10.1016/j.rser.2022.112846>
- Kanaani M, Sedaei B, Asadian-Pakfar M (2022) Role of cushion gas on underground hydrogen storage in depleted oil reservoirs. *J Energy Storage* 45:103783. <https://doi.org/10.1016/j.est.2021.103783>
- Kempka T, Kühn M (2013) Numerical simulations of CO₂ arrival times and reservoir pressure coincide with observations from the Ketzin pilot site, Germany. *Environ Earth Sci* 70:3675–3685. <https://doi.org/10.1007/s12665-013-2614-6>
- Kruck O, Crotogino F, Prelicz R, Rudolph T (2013) Overview on all known underground storage technologies for hydrogen (HyUnder). KBB underground technologies GmbH, Shell International Explorations and Production, E.ON Gas Storage GmbH
- Laille JP, Coulomb C, Tek MR (1986) Underground storage in Cerville-Velaine, France: a case history in conversion and inert gas injection as cushion substitute. In: all days. SPE, New Orleans, Louisiana, p SPE-15588-MS
- Li D, Beyer C, Bauer S (2018) A unified phase equilibrium model for hydrogen solubility and solution density. *Int J Hydrog Energy* 43:512–529. <https://doi.org/10.1016/j.ijhydene.2017.07.228>
- Liebscher A, Martens S, Moller F, Kuhn M (2013) On-shore CO₂ storage at the Ketzin pilot site in Germany. Geological storage of carbon dioxide (CO₂). Elsevier, pp 278–300. <https://doi.org/10.1533/9780857097279.3.278>
- Liu K, Zhu W, Pan B (2024) Feasibility of hydrogen storage in depleted shale gas reservoir: a numerical investigation. *Fuel* 357:129703. <https://doi.org/10.1016/j.fuel.2023.129703>
- Loizzo M, Hennings J, Zimmer M, Liebscher A (2013) Multi-phase equilibrium in a CO₂-filled observation well at the Ketzin pilot site. *Energy Procedia* 37:3621–3629. <https://doi.org/10.1016/j.egypro.2013.06.255>
- Lysy M, Fernø M, Erslund G (2021) Seasonal hydrogen storage in a depleted oil and gas field. *Int J Hydrog Energy* 46:25160–25174. <https://doi.org/10.1016/j.ijhydene.2021.05.030>
- Malki ML et al (2024) OPERATE-H2: a tool for optimizing underground hydrogen storage. *J Energy Storage* 90:111715. <https://doi.org/10.1016/j.est.2024.111715>
- Martens S et al (2012) Europe's longest-operating on-shore CO₂ storage site at Ketzin, Germany: a progress report after three years of injection. *Environ Earth Sci* 67:323–334. <https://doi.org/10.1007/s12665-012-1672-5>
- Medina OE et al (2024) Salinity influence on underground hydrogen storage: insights from molecular dynamics and pore-scale analysis. *Int J Hydrog Energy* 60:959–975. <https://doi.org/10.1016/j.ijhydene.2024.02.073>
- Michelsen J et al (2023) Hydrogen reservoir flow behaviour: measurements of molecular diffusion, mechanical dispersion and relative permeability. H2020 HyUSPre project report, p 67
- Norden B, Förster A (2010) Lithological and petrophysical core-log interpretation in CO₂SINK, the European CO₂ onshore research storage and verification project
- Norden B, Frykman P (2013) Geological modelling of the Triassic Stuttgart formation at the Ketzin CO₂ storage site, Germany. *Int J Greenh Gas Control* 19:756–774. <https://doi.org/10.1016/j.ijggc.2013.04.019>
- Okoroafor ER, Saltzer SD, Kovscek AR (2022) Toward underground hydrogen storage in porous media: reservoir engineering insights. *Int J Hydrog Energy* 47:33781–33802. <https://doi.org/10.1016/j.ijhydene.2022.07.239>
- Oldenburg CM, Finsterle S, Trautz RC (2024) Water upconing in underground hydrogen storage: sensitivity analysis to inform design of withdrawal. *Transp Porous Med* 151:55–84. <https://doi.org/10.1007/s11242-023-02033-0>
- Peng D-Y, Robinson DB (1976) A new two-constant equation of state. *Ind Eng Chem Fund* 15:59–64. <https://doi.org/10.1021/i160057a011>
- Pfeiffer WT, Bauer S (2015) Subsurface porous media hydrogen storage—scenario development and simulation. *Energy Procedia* 76:565–572. <https://doi.org/10.1016/j.egypro.2015.07.872>
- Pfeiffer WT, Beyer C, Bauer S (2017) Hydrogen storage in a heterogeneous sandstone formation: dimensioning and induced hydraulic effects. *Pet Geosci* 23:315–326. <https://doi.org/10.1144/petgeo2016-050>
- Ramesh Kumar K et al (2023) Comprehensive review of geomechanics of underground hydrogen storage in depleted reservoirs and salt caverns. *J Energy Storage* 73:108912. <https://doi.org/10.1016/j.est.2023.108912>
- Raza A et al (2022) A holistic overview of underground hydrogen storage: influencing factors, current understanding, and outlook. *Fuel* 330:125636. <https://doi.org/10.1016/j.fuel.2022.125636>
- Saeed M, Jadhawar P (2024a) Optimizing underground hydrogen storage in aquifers: the impact of cushion gas type. *Int J Hydrog Energy* 52:1537–1549. <https://doi.org/10.1016/j.ijhydene.2023.08.352>
- Saeed M, Jadhawar P (2024b) Modelling underground hydrogen storage: a state-of-the-art review of fundamental approaches and findings. *Gas Sci Eng* 121:205196. <https://doi.org/10.1016/j.jgsce.2023.205196>
- Sainz-Garcia A, Abarca E, Rubi V, Grandia F (2017) Assessment of feasible strategies for seasonal underground hydrogen storage in a saline aquifer. *Int J Hydrog Energy* 42:16657–16666. <https://doi.org/10.1016/j.ijhydene.2017.05.076>
- Sarı E, Çiftçi E (2024a) A numerical investigation on the utilization of a depleted natural gas field for seasonal hydrogen storage: a case study for Değirmenköy gas field. *Int*

- J Hydrog Energy 51:219–228. <https://doi.org/10.1016/j.ijhydene.2023.11.090>
- Sarı E, Çiftçi E (2024b) Underground hydrogen storage in a depleted gas field for seasonal storage: a numerical case study of the Tekirdağ gas field. *Fuel* 358:130310. <https://doi.org/10.1016/j.fuel.2023.130310>
- Schmidt-Hattenberger C et al (2024) Investigation of underground hydrogen storage in a saline aquifer for a prospective demonstrator. *Eur Assoc Geosci Eng*
- Søreide I, Whitson CH (1992) Peng-Robinson predictions for hydrocarbons, CO₂, N₂, and H₂S with pure water and NaCl brine. *Fluid Phase Equilib* 77:217–240. [https://doi.org/10.1016/0378-3812\(92\)85105-H](https://doi.org/10.1016/0378-3812(92)85105-H)
- Sterner M, Specht M (2021) Power-to-gas and power-to-X—the history and results of developing a new storage concept. *Energies* 14:6594. <https://doi.org/10.3390/en14206594>
- Thiyagarajan SR et al (2022) A comprehensive review of the mechanisms and efficiency of underground hydrogen storage. *J Energy Storage* 51:104490. <https://doi.org/10.1016/j.est.2022.104490>
- Wang G, Pickup G, Sorbie K, Mackay E (2022) Numerical modelling of H₂ storage with cushion gas of CO₂ in subsurface porous media: filter effects of CO₂ solubility. *Int J Hydrog Energy* 47:28956–28968. <https://doi.org/10.1016/j.ijhydene.2022.06.201>
- Wang H et al (2023) Numerical study of the efficiency of underground hydrogen storage in deep saline aquifers, rock springs uplift. *Wyo J Clean Prod* 421:138484. <https://doi.org/10.1016/j.jclepro.2023.138484>
- Wasike-Schalling A et al (2023) H2VL—Wasserstoffregion Havelland. Reiner Lemoine Institut GmbH, IAV GmbH, consulting4drive GmbH, Institut für Klimaschutz, Energie und Mobilität e.V
- Yang K et al (2023) Measurement of hydrogen dispersion in rock cores using benchtop NMR. *Int J Hydrog Energy* 48:17251–17260. <https://doi.org/10.1016/j.ijhydene.2023.01.197>
- Zhao Q, Wang Y, Chen C (2024) Numerical simulation of the impact of different cushion gases on underground hydrogen storage in aquifers based on an experimentally-benchmarked equation-of-state. *Int J Hydrog Energy* 50:495–511. <https://doi.org/10.1016/j.ijhydene.2023.07.262>
- Zivar D, Kumar S, Foroozesh J (2021) Underground hydrogen storage: a comprehensive review. *Int J Hydrog Energy* 46:23436–23462. <https://doi.org/10.1016/j.ijhydene.2020.08.138>

Publisher's Note Springer Nature remains neutral with regard to jurisdictional claims in published maps and institutional affiliations.